A continuum approach to combined γ/γ' evolution and dislocation plasticity in Nickel-based superalloys

Ronghai Wu[a], Michael Zaiser[a], Stefan Sandfeld[a,b,*]

[a]*Institute of Materials Simulation, Department of Materials Science, Friedrich-Alexander University of Erlangen-Nürnberg (FAU), Dr.-Mack-Str. 77, 90762 Fürth, Germany*
[b]*Chair of Micromechanical Materials Modelling (MiMM), Institute of Mechanics and Fluid Dynamics, Technische Universität Bergakademie Freiberg (TUBAF), Lampadiusstr. 4, 09596 Freiberg, Germany*

Abstract

Creep in single crystal Nickel-based superalloys has been a topic of interest since decades, and nowadays simulations are more and more able to complement experiments. In these alloys, the γ/γ' phase microstructure co-evolves with the system of dislocations under load, and understanding the mutual interactions is essential for understanding the resulting creep properties. Predictive modeling thus requires multiphysics frameworks capable of modeling and simulating both the phase and defect microstructures. To do so, we formulate a coupled model of phase-field evolution and continuum dislocation dynamics which adequately accounts for both statistically stored and geometrically necessary dislocations. The simulated γ/γ' phase microstructure with four γ' variants and co-evolving dislocation microstructure is found to be in good agreement with experimental observations. The creep strain curve is obtained as a natural by-product of the microstructure evolution equations without the need for additional parameter fitting. We perform simulations of γ/γ' evolution for different dislocation densities and establish the driving forces for microstructure evolution by analyzing in detail the changes in different contributions to the elastic and chemical energy density. Together with comparisons between simulated and experimental creep curves this investigation reveals the mechanisms controlling the process of directional coarsening (rafting) and demonstrates that the kinetics of rafting significantly depends on characteristics of the dislocation microstructure. In addition to rafting under constant load, we investigate the effect of changes in loading conditions and explore the possibility of improving creep properties by pre-rafting along a different loading path.

Keywords: superalloy; creep; phase-field; continuum dislocation dynamics; microstructure

1. Introduction

Single crystal Nickel-based superalloys have been used as high temperature materials already for several decades. They essentially consist of cube-shaped precipitates of an ordered phase (termed γ' phase) embedded in a face-centred cubic, solution hardened matrix (termed γ phase). The atomic microstructure of the coherent $L1_2$ - ordered γ' precipitates renders them strong obstacles to dislocation motion even at elevated temperatures, and optimizing the γ' fraction has played a major role in improving the thermo-mechanical properties of single crystal Ni-based superalloys (Murakumo et al., 2004). Advances in microstructure engineering and manufacturing of single-crystal components have made this class of materials a common choice for components that require good creep resistance at high temperatures, such as turbine blades in jet engines (Davis, 1997). Under typical service conditions the centrifugal force within monocrystal turbine blades is acting parallel to the ⟨001⟩ crystal orientation, which is why superalloy creep (i.e. plastic deformation which occurs at load levels significantly lower than the macroscopically observed yield strength) with the stress axis oriented along a ⟨001⟩ crystal axis has been studied extensively already since the 1970s (see e.g. Tien and Copley, 1971). However, a significant difficulty is posed by the necessity of simultaneously investigating the time dependent aspects of plastic deformation on the macroscopic, specimen scale as well as on the level of the dislocation and phase microstructure. Up to now this is mostly done by interrupting creep tests at distinct times or strain values,

---

*Corresponding author.
Email address:* `stefan.sandfeld@imfd.tu-freiberg.de` (Stefan Sandfeld)

followed by characterizing the respective microstructures (Titus et al., 2015; Wu et al., 2016). However, the picture provided by even the most comprehensive experimental characterization methods is incomplete since it is impossible to directly monitor the dynamic interplay of different microstructural mechanisms and at the same time to obtain detailed information about the internal stresses which provide essential driving forces for both phase (γ/γ') and dislocation microstructure evolution. This, however, is indispensable for understanding the mechanisms that control the evolution of the dislocation and phase microstructure, and that ultimately govern the mechanical material response during (creep) loading.

Simulations, on the other hand, provide full information regarding the evolution of both internal stresses and microstructure morphology on the considered scale of resolution. This may include tensorial stress and strain fields resolved on the scale of the phase microstructure, the geometry of the γ' precipitates, and possibly the evolution and arrangement of dislocations to name but a few. (Obviously, physical details not contained within the respective model *can not* be represented, which therefore requires a careful consideration of the underlying model idealizations). The possibility to control and modify the degree of microstructural detail 'at will' makes such simulations eminently suitable for identifying the mechanisms that govern microstructure evolution and control the microstructure-property relations.

A number of constitutive models on the macroscopic specimen scale have been used to reproduce creep curves (Kim et al., 2016; Oruganti, 2012), without explicitly considering the underlying microstructure evolution. One of the advantages of those models is that they are amenable to numerical implementation within standard finite element frameworks, which are readily available and allow for treatment of complex boundary conditions. These models can be regarded as valuable engineering tools for roughly estimating the creep lifetime (Connolly et al., 2014; Le Graverend et al., 2014). Details of the creep curves are, however, very sensitive with respect to the specific creep test conditions (Reed et al., 1999) – a sensitivity which is particularly pronounced in multi-stage creep processes where the microstructural mechanisms that govern the creep behavior change along the creep curve. As a consequence, not only the model parameters may need to be fitted anew for matching different experimental conditions, but even the constitutive formulation itself may need to be adjusted accordingly. While this might be a feasible approach from an engineering point of view, the predictive power of such models is necessarily limited; such models are reliable only in the very specific situations to which they have been tailored and fitted. In particular, information regarding microstructural processes and creep mechanisms enters such models only in an indirect manner, i.e. through the selection of parameters and the choice of the constitutive model equations, and it is not clear in which precise manner the macroscopic parameters relate to the microstructural processes. This deficiency makes such models, despite their undoubted usefulness as engineering design tools, unsuitable for predictive modeling on the microstructural level and thus for microstructure engineering.

Atomistic methods, such as the molecular dynamics (MD) simulation method are able to show in great detail, for instance, the interaction between edge dislocations and solid solution elements (Zhang et al., 2013). MD simulations have been used to study interface dislocation networks at γ/γ' interfaces (Prakash et al., 2015) and their interactions with matrix dislocations (Wu et al., 2011; Zhu et al., 2013). However, owing to system size limitations, MD simulations can hardly handle large numbers of dislocations or low strain rates, and the intrinsic limitations of the method in capturing slow diffusion-controlled processes make it currently unsuitable for describing the temporal evolution of the phase microstructure.

On the other hand, the discrete dislocation dynamics (DDD) simulation method can not only provide detailed information about dislocations, but can also deal with the evolution of large numbers of dislocations in multiple slip systems on realistic time scales. However, up to now the γ' precipitates in DDD simulations of γ/γ' microstructures have always been assumed to be static: such simulations capture how the precipitates influence the dislocation microstructure evolution but not vice versa (Gao et al., 2015; Huang et al., 2012; Probst-Hein et al., 1999; Yashiro et al., 2006). We demonstrate in the present paper that this may provide a too limited perspective if it comes to understanding creep processes in γ/γ' microstructures, which are determined by the co-evolution of both phase and dislocation microstructures and cannot be reduced to dislocations moving in a static precipitate arrangement.

The phase-field (PF) method has become one of the most popular methods for simulating phase microstructure evolution in a continuum setting. To predict the simultaneous evolution of phase and dislocation microstructure and to study their mutual interactions it is therefore natural to consider also dislocation microstructures – or, more generally speaking, plastic deformation processes – in a continuum setting and couple them

to PF models. In this spirit, phenomenological (visco-) plasticity models have been coupled to mesoscopic PF models, and the results show that plastic activity accelerates rafting (directional coarsening of γ/γ' structure) and causes misalignment of the γ' precipitates (Cottura et al., 2012; Gaubert et al., 2010; Tanimoto et al., 2014; Tsukada et al., 2011). The main disadvantage of these plasticity models is the lack of any information on dislocation microstructure, which limits their ability to reveal dislocation associated mechanisms. By contrast, phase-field dislocation dynamics (PFDD) offers an approach that allows to treat both phase and defect microstructure evolution in a common conceptual framework (Finel and Rodney, 2000; Hu et al., 2004). In this approach, the dislocations on a given slip system are represented by a multiple-valued order parameter where each value represents a quantum of crystallographic slip (slip of a representative slip plane by one Burgers vector). Accordingly, dislocations appear as localized transitions between different values of the slip order parameters. The main problem of the method resides in its computational cost: Since the numerical grid spacing must be sufficiently small to properly resolve the dislocation core, the computational cost of PFDD may become very high, despite attempts to coarsen the PFDD length scale (Rodney et al., 2003). In fact, this approach is rather a continuum formulation of discrete dislocation dynamics, which engenders an additional computational cost because of the need to represent the dislocations by field variables even in locations where they are physically absent – a drawback which needs to be offset against the advantage of being able to treat phase and defect microstructures within a common conceptual framework.

An alternative continuum approach to dislocation plasticity is provided by *Continuum Dislocation Dynamics* (CDD) which defines density measures to characterize the dislocation system and formulates partial differential equations to describe their evolution. This was initiated about half a century ago by Kröner (1958), Nye (1953) and Mura (1963) who introduced a tensorial measure (the so-called *Kröner-Nye tensor*) for the geometrically necessary dislocation (GND) densities inside a crystal, together with the corresponding evolution equations. Up to now, a number of different models, all based on the Kröner-Nye tensor, have been developed including those in (Acharya, 2001; Le, 2016; Sedláček et al., 2003; Xia and El-Azab, 2015). A different line of thought distinguishes dislocations according to their direction of motion and can therefore capture the simultaneous evolution of GND and so-called 'statistically stored' dislocations of zero net Burgers vector. First steps in this direction were taken by Groma (1997); Groma et al. (2003) for a plane-strain geometry with straight edge dislocations. The approach of Groma et al. (2003) is of particular interest for simulation of γ/γ' microstructures since the corresponding evolution equations have been shown by Yefimov et al. (2004) to accurately reproduce the dislocation motions and dislocation-induced internal stress and eigenstrain fields in a precipitation-hardened model material. Subsequently, Hochrainer et al. introduced a very general extension towards arbitrary configurations of curved dislocations (Hochrainer et al., 2014, 2007; Sandfeld et al., 2011, 2015b), which has been successfully benchmarked by discrete dislocations dynamics (DDD) simulations (Sandfeld and Po, 2015) and against a range of other continuum theories (Monavari et al., 2016). The attractiveness of CDD in modeling dislocation microstructure evolution resides in the fact that it allows to treat dislocation microstructures in terms of averages well above the scale of individual dislocations, and can thus achieve a very significant reduction of computational cost not only in comparison with PFDD but also with DDD.

Coupling CDD-type plasticity models and PF models for the evolution of γ/γ' microstructures has only been demonstrated as a proof of concept for an idealized situation in (Wu and Sandfeld, 2016, 2017), where the present authors investigated some aspects of dislocation assisted rafting in terms of the shape evolution of a single γ' precipitate. Thus, collective phenomena in multiple-precipitate coarsening could not be studied. Such collective phenomena arise not only from the direct elastic interactions of multiple precipitates and the superposition of the diffusive fluxes that control precipitate evolution, but equally from the fact that precipitates mutually modulate the dislocation fluxes and dislocation-induced internal stress fields they experience. The ensuing collective phenomena may be essential for understanding the microstructure evolution. In the present work, we develop a model that couples the CDD dislocation dynamics with the PF γ/γ' evolution based on an eigenstrain formalism. Section 2 introduces a PF model which is able to simulate realistic γ/γ' microstructures with four γ' variants. Section 3 details the dislocation density evolution. Section 4 presents numerical results including an analysis of the influence of dislocation associated stresses and associated elastic energy contributions on multi-precipitate coarsening, a discussion of the mechanisms which control local features in the microstructure, microstructure – creep property relations and their dependence on dislocation density, and the possibility of modifying creep properties by pre-deformation along a different loading path. We conclude with a critical discussion of the perspectives and limitations of the present approach in Section 4.

2. The Phase-field model

In single crystal Nickel-based superalloys, the γ' phase has a L1$_2$ crystallographic structure of which there exist four different variants depending on the position of the Al atoms in the unit cell. Suitable PF models for such four-variant γ' microstructures can generally be divided into two different types. The first type considers "physical" order parameters and a realistic interface thickness which is of the order of a few nano meters (Zhu et al., 2004). Therefore, in a numerical implementation a very fine spatial resolution, typically in the sub-nanometer regime, is required. This is also important to avoid artificial 'grid pinning' (De Rancourt et al., 2016). This strongly limits the total size of the domain that can be computed in such a simulation. The second type of models departs from the idea that the real, physical interface is exactly represented in the PF model. There, the interface thickness is rather dictated by numerical properties. To ensure consistency with the underlying physics it is ensured that the simulated interface energy matches the physical interface energy. One of main computational advantages of this approach is that the admissible system size can be significantly extended such that realistic sizes of γ/γ' microstructures can be simulated. The Kim-Kim-Suzuki (KKS) model (Kim et al., 1999), which is used throughout the present work, belongs to this type of models and has been successfully applied to single crystal Nickel-based superalloys (Zhou et al., 2010).

We consider a Ni-Al binary system where the phase microstructure can be represented by one conserved order parameter c characterizing the alloy composition in terms of the local Al concentration, and four non-conserved crystallographic order parameters ϕ_i ($i = 1...4$) which distinguish the four possible γ' variants. Values $\phi_i = 0 \; \forall \; i$ characterize the γ phase, $\phi_i = 1$ for one i denotes the i-variant of the γ' phase and a value $0 < \phi_i < 1$ corresponds to a γ/γ' interface or an interface between different γ' variants, i.e., an antiphase boundary (APB). The evolution of the γ/γ' microstructure is given by equations for the concentration c and the crystallographic order parameters ϕ_i. These equations are derived under the assumption that the rates of change of c and the ϕ_i depend linearly on the corresponding functional derivatives of a free energy functional (Kim et al., 1999). Because the concentration is a conserved quantity and the crystallographic order parameters ϕ_i are non-consered quantities, the corresponding evolution equations are of Cahn-Hilliard and Allen-Cahn type, respectively. Assuming isotropic and homogeneous mobility coefficients M and L we thus find:

$$\partial_t c = M\nabla^2 \frac{\delta F}{\delta c} \quad \text{and} \quad \partial_t \phi_i = -L\frac{\delta F}{\delta \phi_i}. \tag{1}$$

The free energy functional is assumed in the following form:

$$F = \int_V \left[\mathcal{F}^{\text{chem}} + \frac{K_\phi}{2} \sum_{i=1}^{4} |\nabla\phi_i|^2 + \mathcal{F}^{\text{el}} \right] dV, \tag{2}$$

where $\mathcal{F}^{\text{el}}$ and $\mathcal{F}^{\text{chem}}$ are the elastic and chemical contributions to the free energy density and $\frac{1}{2}K_\phi \sum_{i=1}^{4} |\nabla\phi_i|^2$ is a gradient-dependent energy term (with K_ϕ a gradient energy density coefficient). These terms will be detailed subsequently.

2.1. Gradient-dependent energy density

The gradient-dependent energy term $\frac{1}{2}K_\phi \sum_{i=1}^{4} |\nabla\phi_i|^2$ in Eq. (2) controls the structure of the inter-phase boundaries. This contribution is treated in the spirit of phenomenological phase field modeling: Given a functional form for the chemical free energy and assuming a computational interface thickness and numerical resolution, the gradient energy parameter K_ϕ is adjusted such that it reproduces the correct interface energy. The interface energy can be obtained from other calculation methods such as cluster variation method (Wang et al., 2007). The value of the parameter K_ϕ thus needs to be determined once the other energy contributions are specified.

2.2. Chemical free energy density

The local chemical free energy density $\mathcal{F}^{\text{chem}}$ governs the energy of a mixture of the γ and γ' phases. It is linked to the chemical free energy of the γ and γ' phases by:

$$\mathcal{F}^{\text{chem}} = \left(1 - h(\phi_1,...,\phi_4)\right)\mathcal{F}^\gamma + h(\phi_1,...,\phi_4)\mathcal{F}^{\gamma'} + \mathcal{G}(\phi_1,...,\phi_4) \tag{3}$$

where $h(\phi_1,\ldots,\phi_4)$ is an interpolation function introduced below, and the free energies of the γ and γ' phase, $\mathcal{F}^\gamma$ and $\mathcal{F}^{\gamma'}$, are given by

$$\mathcal{F}^\gamma = F_0(c_\gamma - c_\gamma^e)^2 \quad \text{and} \quad \mathcal{F}^{\gamma'} = F_0(c_{\gamma'} - c_{\gamma'}^e)^2. \tag{4}$$

Therein, F_0 is the second derivative of the chemical free energy near the equilibrium composition, c_γ and $c_{\gamma'}$ are the concentrations of Al in the γ and γ' phases, and and c_γ^e and $c_{\gamma'}^e$ are the respective equilibrium concentrations. Local equilibrium requires $\mathrm{d}\mathcal{F}^\gamma/\mathrm{d}c_\gamma = \mathrm{d}\mathcal{F}^{\gamma'}/\mathrm{d}c_{\gamma'}$, hence $c_\gamma - c_{\gamma'} = c_\gamma^e - c_{\gamma'}^e$. From the Al concentrations in the components of the local $\gamma - \gamma'$ mixture, the overall concentration is evaluated with the same interpolation function $h(\phi_1,\ldots,\phi_4)$ as used for the chemical free energy:

$$c = [1 - h(\phi_1,\ldots,\phi_4)]\,c_\gamma + h(\phi_1,\ldots,\phi_4)\,c_{\gamma'}. \tag{5}$$

The interpolation function h is assumed to take the following form

$$h(\phi_1,\ldots,\phi_4) = \sum_{i=1}^{4}[\phi_i^3(6\phi_i^2 - 15\phi_i + 10)]. \tag{6}$$

This choice ensures that h fulfills the following conditions:

- $h = 0$ and $\nabla_\phi h = 0$ if $\phi_i = 0 \; \forall \; i$,

- $h = 1$ and $\nabla_\phi h = 0$ if $\phi_i = 1$ and $\phi_j = 0 \; \forall \; i \neq j$ (a pure variant).

The different crystallographic variants of the order parameter ϕ are distinguished by the free energy contribution $\mathcal{G} = G_\phi g(\phi_1,\ldots,\phi_4)$ where the function $g(\phi_1,\ldots,\phi_4)$ is assumed as

$$g(\phi_1,\ldots,\phi_4) = \sum_{i=1}^{4}\phi_i^2(1 - \phi_i^2) + \theta \sum_{i,j=1}^{4}\phi_i^2\phi_j^2. \tag{7}$$

The non-dimensional parameter θ penalizes co-existence of different variants and thus relates to the APB energy. We choose this parameter in a phenomenological manner such that the APB energy exceeds the γ/γ' phase boundary energy by a factor > 2, thus preventing coalescence of different γ' variants. Finally, the dimensional energy parameter G_ϕ is chosen such as to reproduce, in conjunction with the gradient energy parameter K_ϕ, the correct value for the γ/γ' interface energy.

Note that we do not consider a direct energetic coupling between the dislocation state and the crystallographic order parameters ϕ_i. Such a coupling is in principle provided by the APB energy (a γ dislocation moving into γ' trails an APB) and would require a more physically accurate treatment of APB effects. The implications of this simplification will be discussed in the Conclusions.

2.3. Elastic energy density

The elastic free energy density plays a key role in our model because it provides a long-range coupling between different precipitates, and also between the dislocation and the phase microstructure. There are different ways of introducing the elastic energy into a phase field model. Traditionally, the phase field community states the problem in terms of Khachaturyan's elastic energy functional (Khachaturyan, 1983) which derives from solving the elastic eigenstrain problem specified below by using a Green's function method to solve the stress equilibrium equation. This approach works only for infinite, elastically homogeneous systems (in simulations: for periodic boundary conditions). In the plasticity community, on the other hand, the elastic energy is normally formulated using the (plastic) eigenstrain formalism (Sandfeld et al., 2013), and evaluations are based on the finite element methodology. Both formulations are equivalent in situations where Khachaturyan's formulation applies, however, the eigenstrain formalism has the advantage that it can be applied straightforwardly to finite systems and is readily generalized to account for elastic heterogeneity. We therefore state the elastic energy in terms of an eigenstrain formulation.

In the following we use bold symbols for vectors or second order tensors, and non-bold symbols for scalar values. The symmetrized version of a second-rank tensor X is denoted by $X^{(s)}$, the symbol $\otimes$ denotes the outer

(tensor) product, a dot "·" denotes the inner product and ":" is the double inner product. With these notations, the elastic energy density is given by:

$$\mathcal{F}^{\text{el}} = \frac{1}{2}\boldsymbol{\sigma} : \boldsymbol{\varepsilon}^{\text{el}} \tag{8}$$

where the elastic strain $\boldsymbol{\varepsilon}^{\text{el}}$ and the stress $\boldsymbol{\sigma}$ are linked through the fourth order stiffness tensor $\mathbb{C}$,

$$\boldsymbol{\sigma} = \mathbb{C} : \boldsymbol{\varepsilon}^{\text{el}}. \tag{9}$$

In Ni-based superalloys, the γ and γ' phases have slightly different elastic constants. This elastic inhomogeneity may in principle affect the directional coarsening behavior (Gaubert et al., 2010; Gururajan and Abinandanan, 2007). In the following we neglect the elastic inhomogeneity and use the same stiffness tensor $\mathbb{C}$ for the γ and γ' phases. This simplification is *not* motivated by computational convenience – since we use a finite element method for solving the eigenstrain problem, implementation of elastic heterogeneity would be straightforward. Our motivation rather stems from the fact that, for an elastically homogeneous microstructure, no directional coarsening occurs in the absence dislocation motion and plastic flow. Thus, the assumption of elastic homogeneity allows us to systematically elucidate the role played by dislocation motion in directional coarsening without the need to disentangle dislocation effects from superimposed effects of elastic heterogeneity.

Given that both misfit strains and typical creep strains are small, we adopt a small-strain formulation. The total strain $\boldsymbol{\varepsilon}$ then derives from the material displacement vector $\boldsymbol{u}$ according to

$$\boldsymbol{\varepsilon} = (\nabla \otimes \boldsymbol{u})^{(\text{s})} \tag{10}$$

The strain tensor is now additively decomposed into an elastic strain $\boldsymbol{\varepsilon}^{\text{el}}$ and an inelastic (or eigen-)strain $\boldsymbol{\varepsilon}^{\text{inel}}$. The latter is the sum of eigenstrains due to the γ/γ' lattice misfit, $\boldsymbol{\varepsilon}^{\text{mis}}$, and eigenstrains caused by dislocation-mediated plastic deformation, $\boldsymbol{\varepsilon}^{\text{dis}}$. It follows for the elastic strain tensor:

$$\boldsymbol{\varepsilon}^{\text{el}} \quad = \quad \boldsymbol{\varepsilon} - \boldsymbol{\varepsilon}^{\text{inel}} = (\nabla \otimes \boldsymbol{u})^{(\text{s})} - (\boldsymbol{\varepsilon}^{\text{mis}} + \boldsymbol{\varepsilon}^{\text{dis}}). \tag{11}$$

The two eigenstrain tensors are given by

$$\boldsymbol{\varepsilon}^{\text{mis}} \quad = \quad h(\phi_1, \dots, \phi_4)\epsilon^{\text{mis}}\mathbf{I} \tag{12}$$

$$\boldsymbol{\varepsilon}^{\text{dis}} \quad = \quad \sum_k a^k \boldsymbol{M}^k, \tag{13}$$

where ϵ^{mis} is the volumetric eigenstrain due to γ/γ' lattice misfit, $\mathbf{I}$ is the second order unit tensor, a^k is the scalar shear strain on the k-th crystallographic slip system, and the projection tensor $\boldsymbol{M}^k$ characterizes the respective shear direction. Both a^k and $\boldsymbol{M}^k$ will be defined and discussed in the following section.

Minimization of the elastic energy functional with respect to the displacement field $\boldsymbol{u}$ leads to the mechanical equilibrium equation

$$\nabla \cdot \boldsymbol{\sigma} = \mathbf{0} \tag{14}$$

which has to be solved in the system domain accounting for the imposed Dirichlet or Neumann boundary conditions for the displacement field $\boldsymbol{u}$ in order to evaluate, via Eqs. (9) and (8), the elastic energy.

3. The Continuum Dislocation Dynamics model

In the following we formulate the plastic deformation problem following the work of Groma et al. (2003) and Yefimov et al. (2004). Deformation can occur by crystallographic slip on several slip systems i characterized by Burgers vectors $\boldsymbol{b}^k$ of modulus b, corresponding slip vectors $s^k = \boldsymbol{b}^k/b$, and slip plane normals $\boldsymbol{n}^k$ where $\boldsymbol{n}^k \cdot \boldsymbol{b}^k = 0$. We consider a two-dimensional plane strain setting where all $\boldsymbol{b}_k$ and $\boldsymbol{n}_k$ are contained in the xy plane and deformation is homogeneous in z direction. The plastic strain tensor can then be written as

$$\boldsymbol{\varepsilon}^{\text{dis}} = \sum_k \boldsymbol{M}^k a^k \quad \text{with} \quad \boldsymbol{M}^k = (s^k \otimes \boldsymbol{n}^k)^{(\text{s})}. \tag{15}$$

Owing to the homogeneity in z direction, the dislocation system consists of positive and negative edge dislocations with Burgers vectors $\boldsymbol{b}_i$. The line direction of all dislocations is perpendicular to the xy plane. We use a

density-based formulations where positive and negative dislocations are represented by densities $\rho^{+,k}$ and $\rho^{-,k}$ which can simply be understood as averaged numbers of dislocations, of a given slip system k, per unit area in the xz plane. From the sign-dependent densities $\rho^{\pm,k}$ the total dislocation density ρ^k of each slip system can be calculated as $\rho^k = \rho^{+,k} + \rho^{-,k}$, the excess (signed GND) dislocation density is evaluated as $\kappa^k = \rho^{+,k} - \rho^{-,k}$, and the Kröner-Nye tensor is $\boldsymbol{\alpha}^k = \kappa^k(\boldsymbol{b} \otimes \boldsymbol{e}_z)$.

3.1. The CDD transport equations

Dislocations move in such a manner as to reduce the elastic energy. We consider glide motion where positive and negative dislocations of slip system k move along the $\boldsymbol{s}^k$ direction with the respective velocities $\boldsymbol{v}^{k,\pm} = \pm \boldsymbol{s}^k v_g^k$. This motion produces a resolved shear strain a^k with the local strain rate

$$\partial_t a_k(\boldsymbol{r}, t) = (\rho^{+,k}(\boldsymbol{r}, t) + \rho^{-,k})v_g^k(\boldsymbol{r}, t)b. \tag{16}$$

At the same time, motion of dislocations implies their spatial transport and thus a spatio-temporal evolution of the dislocation microstructure. Following Groma et al. (2003) and Yefimov et al. (2004) we consider the simplest possible transport model where the densities $\rho^{\pm,i}$ are considered as conserved quantities such that the dislocation density kinetics is described by the simple continuity equations

$$\partial_t \rho^{+,k} = \nabla(\boldsymbol{v}_g^{+,k}\rho^{+,k}) = (\nabla.\boldsymbol{s}^k)(v_g^k\rho^{+,k}), \tag{17}$$

$$\partial_t \rho^{-,k} = \nabla(\boldsymbol{v}_g^{-,k}\rho^{-,k}) = -(\nabla.\boldsymbol{s}^k)(v_g^k\rho^{-,k}), \tag{18}$$

where spatial derivatives are evaluated along the respective local glide directions $\boldsymbol{s}^k$.

To complete the CDD framework, the dislocation velocities need to be related to the thermodynamic driving forces for dislocation glide and possibly also to the variables characterizing the dislocation state. In principle, the thermodynamic driving force for dislocation glide on slip system k is provided by the resolved shear stress $\tau^k = \boldsymbol{M}^k : \boldsymbol{\sigma}$ which is work conjugate to the shear strain a^k. However, on the level of dislocation density evolution, the simple assumption of a proportionality between (average) resolved shear stress and dislocation velocity has long been proven inadequate for capturing the evolution of dislocation densities in confined geometries even where such a proportionality exists on the single-dislocation level (Groma et al., 2003). Thus, more complex velocity relationships need to be formulated.

Several approaches are available to this end: (i) Averaged velocities for dislocation densities can be obtained by direct averaging of the discrete equations of motion. This approach was proposed by Groma (1997) and elaborated by Groma et al. (2003) and recently by Valdenaire et al. (2016). (ii) Velocities can be derived from a free energy functional which contains statistically averaged, dislocation-density dependent stored energy contributions. Averaged elastic energy functionals for dislocation systems were recently derived by Zaiser (2015), and in Groma et al. (2016) it was demonstrated that velocity expressions which derive from variation of such functionals can be matched to those obtained by direct averaging of the discrete dislocation dynamics. (iii) A more conventional method consists in simply postulating, in the spirit of phenomenological plasticity modeling, constitutive relationships between the dislocation velocities, the resolved shear stress, and the dislocation densities in such a manner as to match obervations or, on scales where direct observations are hard to come by, to reproduce behavior found in discrete dislocation dynamics simulations. This is the approach we use in the following.

Our model is designed to reproduce dislocation behavior in situations where the motion of dislocations is over-damped and the glide velocity of an individual dislocation i in slip system k is proportional to the resolved shear stress acting on that dislocation, $v(\boldsymbol{r}_i) = B\tau^k(\boldsymbol{r}_i)$. The mobility coefficient B is taken to account for the influence of the phase microstructure on dislocation motion: as experimental observations show that dislocations cannot move into γ' precipitates until the last stage of creep, whereas our current work focuses on the early creep stages, we evaluate the effective dislocation mobility using a rule of mixtures as $B = B^\gamma[1 - h(\phi_1, \ldots, \phi_4)] + B^{\gamma'}h(\phi_1, \ldots, \phi_4)$ where $B^{\gamma'} \approx 0$. Thus, we assume that the effective mobility of dislocations, and hence the dislocation velocity, is zero in the γ' phase.

3.2. Constitutive equation with Taylor-type yield stress

Upon averaging, the stress acting on a single dislocation is replaced by the average stress acting on dislocations in any given volume element. In performing the average, some caution is needed since the presence of

Table 1: Parameters used in our simulations (partially taken from (Zhou et al., 2010))

c_γ^e [-]	$c_{\gamma'}^e$ [-]	f_0 [J m^{-3}]	k_ϕ [J m^{-1}]	ω [J m^{-3}]	θ [-]	M [m^5 J^{-1}]	L [m^3 J^{-1}]
0.160	0.229	3.2×10^9	9.4×10^{10}	3.9×10^6	10	1.5×10^{-26}	5.8×10^{-9}
D [-]	α [-]	C_{11} [GPa]	C_{12} [GPa]	C_{44} [GPa]	$\bar{\epsilon}^{\mathrm{mis}}$ [-]	b [nm]	B [GPa s]
0.6	0.2	198	138	97	-0.003	0.25	1×10^{-13}

correlations in the dislocation arrangement implies that the average stress controlling the dislocation velocity is *not* simply equal to the spatial average. Instead, a careful calculation demonstrates that the average stress acting on dislocations can be represented as a sum of several contributions (Groma et al., 2003, 2016; Valdenaire et al., 2016) among which: (i) the local resolved shear stress $\tau^k = \boldsymbol{M}^k : \boldsymbol{\sigma}$; (ii) a back stress $\tau^{\mathrm{b},k}$ which is proportional to the gradient of the excess dislocation density κ^k; (iii) a Taylor-type yield stress $\tau^{\mathrm{y},k}$ which acts as a "friction stress". We assume the same velocity function v_g^k for positive and negative dislocations. It takes the form

$$v_g^k = \begin{cases} B \, \mathrm{sign}(\tau^k + \tau^{\mathrm{b},k})(|\tau^k + \tau^{\mathrm{b},k}| - \tau^{\mathrm{y},k}) & \text{if } |\tau^k + \tau^{\mathrm{b},k}| > \tau^{\mathrm{y},k}, \\ 0 & \text{else.} \end{cases} \tag{19}$$

$$\tau^k = \boldsymbol{\sigma} : \mathcal{M}, \quad \tau^{\mathrm{b},k} = -\frac{DGb}{\rho} \boldsymbol{s}^k \cdot \nabla \kappa^k, \quad \tau^{\mathrm{y},k} = \alpha Gb \sqrt{\rho}. \tag{20}$$

Here, B is a dislocation mobility coefficient, G is the shear modulus, $\alpha = 0.2\ldots0.4$ and $D = 0.6\ldots1$ are two material independent, dimensionless coefficients, and the total dislocation density is given by $\rho = \sum_k(\rho^{+,k} + \rho^{-,k})$.

4. Rafting - simulation results and discussion

4.1. Simulation setup and numerical methods

We perform creep deformation simulations for a two-dimensional system deforming in plane strain, imposing periodic boundary conditions for all fields. The boundaries of the square simulation box are aligned with the axes of a Cartesian coordinate system which is rotated with respect to the cubic crystal axes in such a manner that the [10] cubic crystal axis is aligned with the diagonal of the coordinate system, $\boldsymbol{e}_{[10]} = (\boldsymbol{e}_x + \boldsymbol{e}_y)/\sqrt{2}$, see Fig. 1(a). Creep deformation is induced by a spatially homogeneous and temporally constant tensile stress $\sigma^{\mathrm{ext}} = 200$ MPa acting along the cubic axis in $\boldsymbol{e}_{[10]}$ direction. This direction is henceforth in our discussion referred to as 'parallel' direction whereas $\boldsymbol{e}_{[01]}$ indicates the 'perpendicular' direction. We assume two slip equivalent slip systems with the respective slip plane normals $\boldsymbol{n}_I = \boldsymbol{e}_y$ and $\boldsymbol{n}_{II} = \boldsymbol{e}_x$ and slip directions $\boldsymbol{s}_I = \boldsymbol{e}_x$ and $\boldsymbol{s}_{II} = -\boldsymbol{e}_y$ which correspond to [11] and [1$\bar{1}$] lattice directions. The external stress $\sigma^{\mathrm{ext}} = 200$ MPa leads in the two symmetrically inclined slip systems to equal resolved shear stresses of magnitude $\tau^{\mathrm{ext}} \approx 100$ MPa. The system is homogeneous in z direction.

The material parameters used in our simulations are typical of NiAl γ/γ' microstructures; elastic constants and thermodynamic parameters of the phase field model refer to a deformation temperature of $T = 1253$ K. A compilation of all parameters is provided in Tab. 1.

To evaluate the elastic energy and stress state, we proceed in two steps. In a first step, we solve the elastic eigenstrain problem for an infinite body without boundary tractions. Bulk behavior is mimicked by imposing periodic boundary conditions on the simulation domain. Unlike the strain-based method of evaluating the stress and elastic energy from the eigenstrain using a Green's function method, the displacement-based finite element formulation used in our simulations entails a technical subtlety: By imposing periodic Dirichlet boundary conditions for the displacements, the spatial average of the total strain is by construction set equal to zero. As a consequence, the spatial average of the elastic strain, or equivalently the internal stress, cannot be zero once inelastic eigenstrains of non-zero spatial average are present. Because of the requirement of macroscopic stress equilibrium, however, a non-zero average of the internal stress is inconsistent with the absence of boundary tractions. This problem can be resolved in a simple manner by subtracting the average eigenstrain value $\langle \boldsymbol{\epsilon}^{\mathrm{inel}} \rangle = \langle \boldsymbol{\epsilon}^{\mathrm{mis}} + \boldsymbol{\epsilon}^{\mathrm{dis}} \rangle$ from the elastic strain in a post-processing step (cf. Nemat-Nasser and Hori, 1999; Sandfeld et al., 2015a), i.e., we set

$$\boldsymbol{\sigma} = \mathbb{C} : (\boldsymbol{\epsilon}^{\mathrm{el}} - \langle \boldsymbol{\epsilon}^{\mathrm{inel}} \rangle). \tag{21}$$

where ϵ^{el} is the elastic strain calculated from the displacement field with periodic Dirichlet conditions. As a result of the correction, the evaluated elastic strains and eigenstresses now have zero spatial average, as they should, and correctly represent the solution of the eigenstrain problem in an infinite body without boundary tractions. In a second step we then use the superposition principle to add the spatially constant external stress σ^{ext}, and correct the elastic energy accordingly.

In our simulations we use a simple cubic grid with equally-sized cubic elements and a grid spacing of 20 nm. The model equations are non-dimensionalized by using the grid spacing to scale all lengths, using a time constant of 0.7 s and an energy scale of $1 \times 10^9 \, \text{J m}^{-3}$. The simulation domain is $2.56 \, \mu\text{m} \times 2.56 \, \mu\text{m}$ in size. For solving the elastic problem (14) we use the finite element method with quadratic interpolation functions. For the phase field model as well as for the CDD problem we use the finite volume method (FVM), implemented with a first-order implicit Euler scheme. It is worth mentioning that the time scale of CDD is much smaller than the time scale of PF, because dislocations move much faster than the γ/γ' interfaces evolve. We therefore use a staggered scheme where, between two PF time steps, dislocations may evolve for many CDD time steps until a quasi-static dislocation configuration is reached.

The initial γ/γ' microstructure for rafting is generated by precipitation from a supersaturated solution with $c = 0.204 + R$ and $\phi_i = 0.25 + R$ where R is a small Gaussian fluctuation term. The four different γ' variants are subsequently indicated by four different colors as shown in Fig. 1(b). The average dislocation density for each of the two slip systems in our simulations is ρ_0 in the γ phase and zero in the γ' phase, and we assume that initially the excess (GND) density is zero. Thus our initial conditions for the dislocation densities are generated from the initial precipitate microstructure by setting $\rho^k(\boldsymbol{r}) = \rho_0[1 - h(\phi_1, \ldots, \phi_4)]$ and $\kappa^k(\boldsymbol{r}) = 0$.

4.2. Creep simulation with and without dislocations

The first set of simulations is performed without dislocations ($\rho_0 = 0$) in order to obtain reference data. As shown in Fig. 1(b) and (d), γ' precipitates are coarsening either by consuming small precipitates (grey-dashed box I) or by merging adjacent precipitates of the same variant (grey-dashed box II), which is energetically favorable due to the reduction of interface energy. Different γ' variants, however, can not merge since the APB energy between them is higher than twice the γ/γ' interface energy. The γ' coarsening is non-directional because of the absence of elastic inhomogeneity.

A second set of simulations is performed with finite dislocation density, assuming for the dislocation density in the γ channels the typical value $\rho_0 = 1 \times 10^{13} \, \text{m}^2$. The simulations are started from the same phase microstructure as before and Fig. 1(c) shows the evolved microstructure at the same time step as Fig. 1(d). As creep proceeds, γ' precipitates now preferentially coarsen in the direction perpendicular to the stress axis. This directional coarsening proceeds through two different mechanisms: (i) some precipitates immediately coarsen into the perpendicular direction, as marked by the black, dashed box I in Fig. 1(d). This coarsening mechanism is similar to the one that was observed by the authors for the case of a single precipitate (Wu and Sandfeld, 2016, 2017). (ii) another coarsening mechanism consists in dislocations accelerating the merger of γ' precipitates of the same variant which are, even at some distance, mutually aligned perpendicular to the stress axis: see the precipitates marked by black-dashed boxes II.

4.3. Evolution of dislocation densities and stresses

To reveal why and how the dislocation arrangement evolves during creep, it is necessary to take a closer look at details of the dislocation patterns as shown in Fig. 2 at the initial time step and Fig. 3 after 1×10^4 s. The color bars are the same as in Fig. 2 and Fig. 3 in order to make the results easier comparable. Initially, only SSDs are present, the excess dislocation density is negligible, and the plastic strain is zero everywhere (see Fig. 2(b,c)).

The long range shear stress is the sum of resolved stresses due to external loading, γ/γ' misfit eigenstrain and dislocation eigenstrain. Initially, the dislocation eigenstrain is negligible and the stress field arises from superposition of the external stress and the stress associated with the γ/γ' misfit. In the channels that are perpendicular to the stress axis, this stress adds to the external stress whereas, in the channels parallel to the stress axis, the contributions subtract. As a consequence, the shear stress in the perpendicular channels is positive (200 MPa), while in parallel channels we find a negative value of about -40 MPa (see Fig. 2(d)). The initial back stress, which is proportional to the gradient of the excess dislocation density, is negligible due to the low initial excess dislocation density (see Fig. 2(e)). The initial SSD dislocation configuration results in a uniform yield stress of about 40 MPa in the γ channels (see Fig. 2(f), note that the γ' precipitates, where the
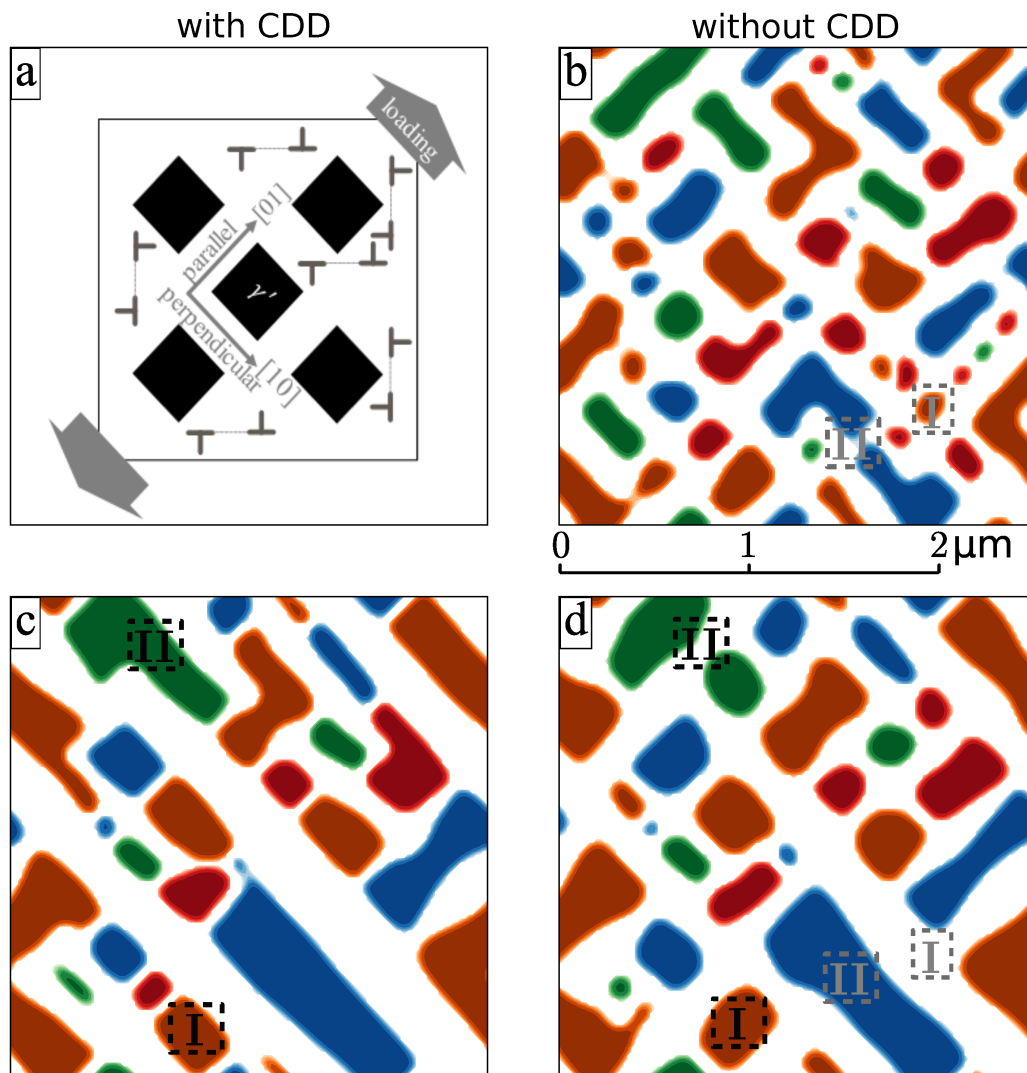
Figure 1: Comparison of γ/γ' morphology with and without CDD: (a) schematic representation of the system; (b) initial state; (c) intermediate state evolving under the influence of dislocation motions; (d) intermediate state without dislocations.

dislocation mobility is zero, are marked in dark grey on this plot). Since the yield stress in the perpendicular channels is below the long range shear stress, dislocations can move. In the parallel channels, by contrast, the magnitudes of the long range shear stress and the yield stress are comparable, which implies dislocations are significantly less active. Positive dislocations move in the positive slip direction under the action of a positive stress and in the negative slip direction under a negative stress, while the opposite is the case for negative dislocations. Hence, during creep, positive and negative dislocations separate in the perpendicular channels as they accumulate at the γ/γ' interfaces, while such separation is not obvious in the parallel channels (see Fig. 3(b)). This agrees with experimental observations (Jácome et al., 2013; Miura et al., 2000). The plastic strain distribution shows that massive dislocation motion has taken place in the perpendicular but not in the parallel γ channels (see Fig. 3(c)). The long range shear stress is altered not only because of the γ/γ' morphology change but also because of the changes in the dislocation configuration which correspond to the piling up of geometrically necessary dislocations at the γ/γ' interfaces. The dislocation pileups counter-act the joint action of external and misfit stresses as they reduce the magnitude of the long range shear stress in the perpendicular channels, while they increase its magnitude in the parallel channels, however, this effect is comparatively modest (compare Figs. 2(d) and Fig. 3(d)). A more important role is played by the short-range mutual repulsion of GNDs which is represented by the back stress, which acts as resistance to the formation of dislocation pile-ups and plays the main role in offsetting the long-range stresses in the perpendicular channels (see Fig. 3(e)). This finding corroborates the earlier conclusion of Groma et al. (2003) who demonstrated by comparison of CDD and DDD data for the deformation of a single slip channel that back stresses related to short-range GND repulsion can, even in the absence of dislocation-related long range stresses, explain the distribution of slip in constrained channels and the related size effects. Finally we note that the motion of dislocations depletes the perpendicular channels where the local flow stresses are small, whereas in the parallel channels, where little dislocation motion occurs, the yield stress remains close to its initial value and remains dominated by SSD interactions.
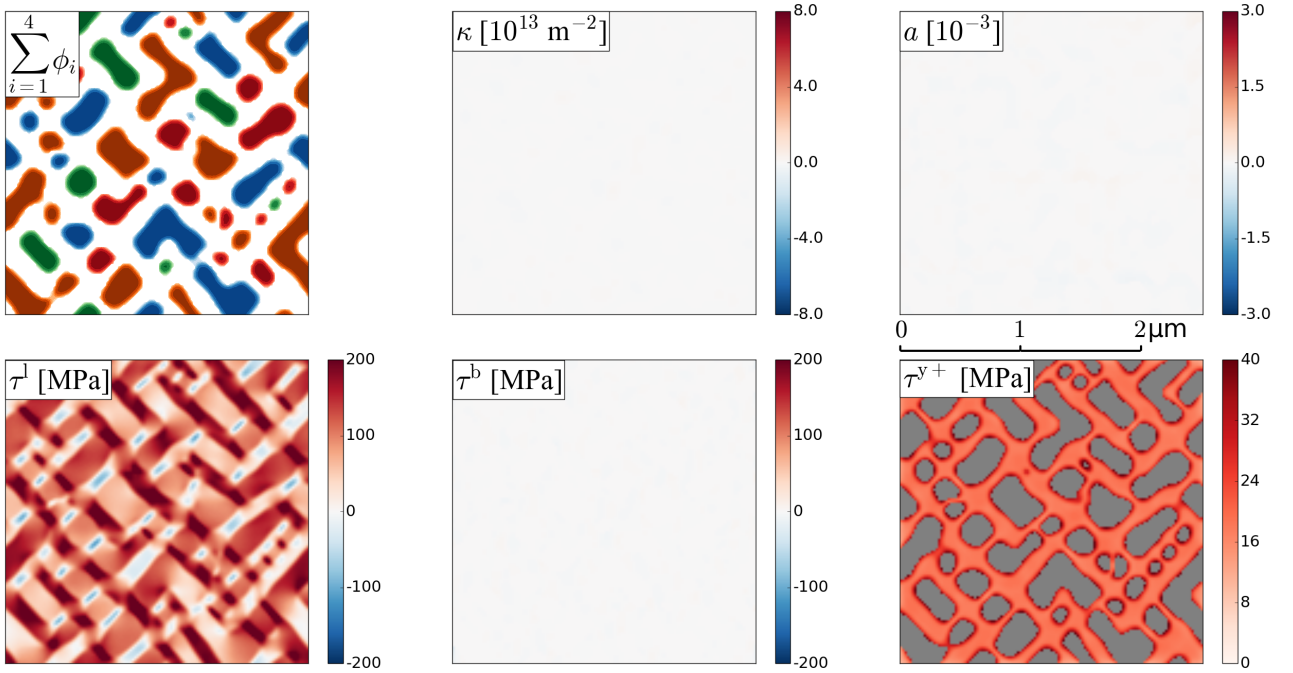

Figure 2: Fields at initial state: (a) γ/γ' morphology; (b) excess density; (c) plastic strain; (d) long range stress; (e) back stress; (f) yield stress.

4.4. Dislocation density dependence of γ/γ' microstructure evolution and creep properties

Accurate measurement of dislocation densities which could be used to define initial data for our simulations is still challenging. The dislocation density in single crystal Nickel-based superalloys is observed to be $5 \times 10^{12} \sim 5 \times 10^{13}$ m^{-2} initially and increases to $5 \times 10^{13} \sim 5 \times 10^{14}$ at γ/γ' interfaces when creep proceeds (Jácome et al., 2013; Miura et al., 2000; Nörtershäuser et al., 2015). In 3D γ/γ' microstructures dislocation
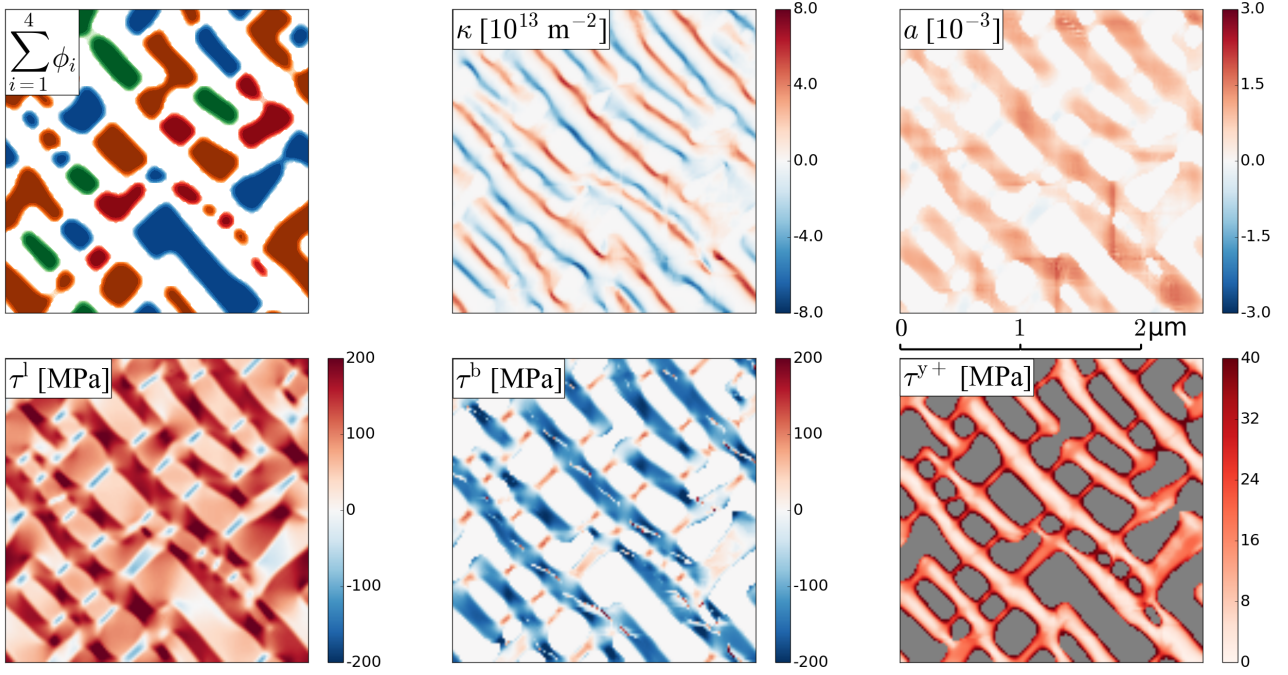
Figure 3: Fields at intermediate state: (a) γ/γ' morphology; (b) excess density; (c) plastic strain; (d) long range stress; (e) back stress; (f) yield stress.

multiplication, leading to an increase in overall dislocation density, proceeds by expansion of loops within the γ channels, and consequential deposition of GNDs at the γ/γ' interfaces. While this behavior can be well captured by 3D CDD simulations (see Monavari et al. (2016) as an example), in our 2D simulations dislocations are assumed straight and therefore dislocation multiplication cannot occur. In principle it is possible to remedy this problem by introducing dislocation sources (see e.g. Yefimov et al. (2004)), however, this would require us to make phenomenological and to some extent arbitrary assumptions regarding source properties. Instead, we investigate the influence of an increasing dislocation density by comparing simulations carried out for three different initial dislocation densities (5×10^{12}, 1×10^{13} and 5×10^{13} m^{-2}). The γ/γ' morphology and total dislocation density fields after 5.6×10^4 s creep time are compared in these three cases, as shown in Fig. 4.

As the dislocation density increases, the resulting γ/γ' morphologies show some gradual changes. First of all, in simulations with increased dislocation density, some small precipitates tend to be retained, such as the precipitates marked by the black-dashed boxes I in Fig. 4. Secondly, the presence of high dislocation densities favors the formation of connected channels in the perpendicular direction. As a consequence, precipitates which are elongated in parallel direction and block such channels, may be split in two (see black-dashed boxes II in Fig. 4). Moreover, while initially all γ/γ' boundaries are basically aligned with the [01] or [10] orientation, local misalignment starts to appear in simulations at high dislocation density, see black-dashed boxes III in Fig. 4. Last but not least, the extent of rafting increases as the dislocation density increases and more dislocations pile up at γ/γ' interfaces. Thus the bottom-line is that increasing the dislocation density promotes directional rafting but may, to some extent, counter-act coarsening.

The simulated evolution of plastic creep strain with time is plotted together with experimental data at 1253 K and 200 MPa (Link et al., 2000). From the plots in Fig. 5, left, one can observe that the strain does not simply scale with the number of dislocations, but exhibits a non-trivial dependency on dislocation density. The creep rate in our simulations is in the first simulation steps very high, as dislocations separate and move across the γ channels to pile up against the γ/γ' interfaces, producing a quasi-instantaneous creep strain. This piling up leads to significant back stresses which shut down rapid dislocation flow in the γ channels and lead to a quasi-stationary state where further creep is controlled by the slow co-evolution of the phase and defect microstructure (motion of the γ/γ' interfaces and concomitant dislocation motions in the γ channels). Due to the absence of dislocation multiplication and recovery mechanisms in our model we do not reach a quasi-stationary regime of constant strain rate (secondary creep) in our simulations. Nevertheless, simulations with a dislocation density of $\rho_0 = 5 \times 10^{13}$ m^{-2}, which is comparable to experimentally observed dislocation densities

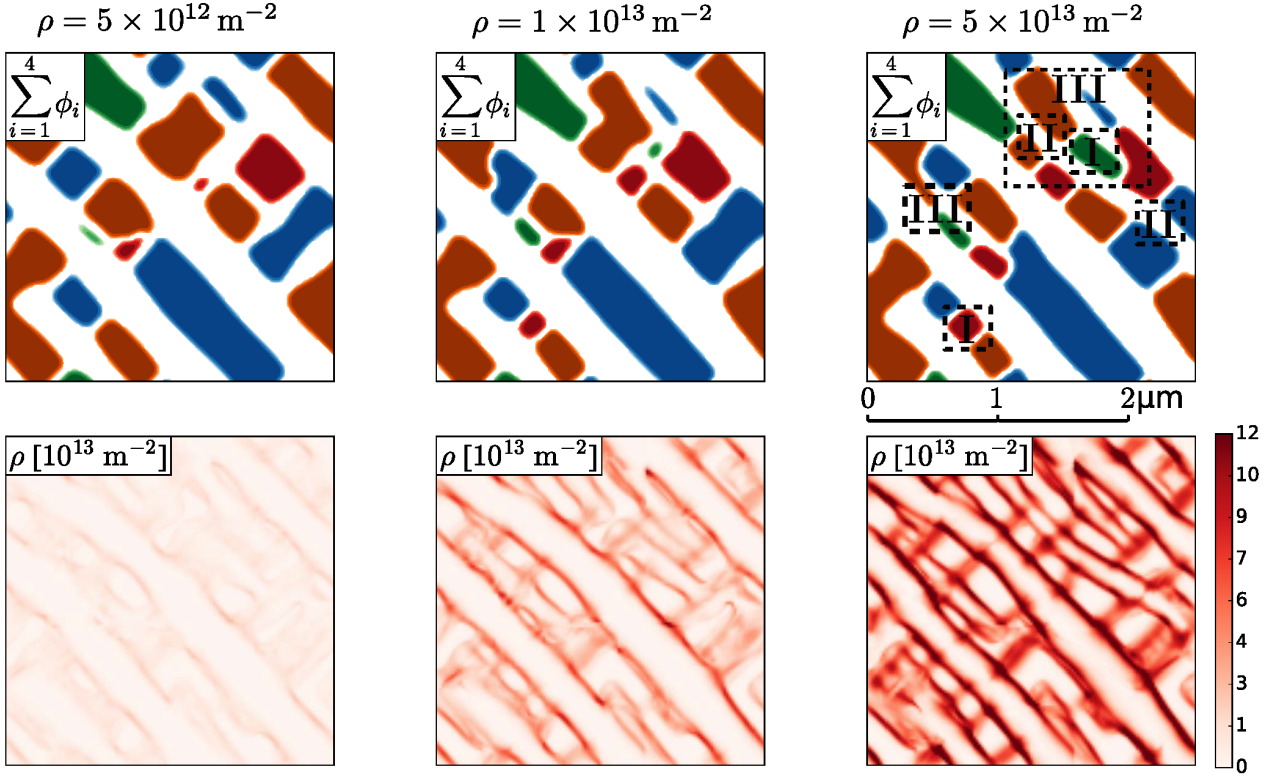Figure 4: Comparison of γ/γ' morphology (a)-(c) and total dislocation density (d)-(f) at 5.6×10^4 s with different initial dislocation densities: (a) and (d) 5×10^{12} m^{-2}; (b) and (e) 1×10^{13} m^{-2}; (c) and (f) 5×10^{13} m^{-2}.

in the secondary creep regime, produce acceptable quantitative agreement with experimental data.

While the creep process and to a lesser extent the directional coarsening morphology depend on dislocation density, the coarsening process itself (i.e., the widening of the channels and the growth of the precipitates) is practically not affected by dislocation activity. This process, which is driven by interface energy reduction, follows the classical $t^{1/2}$ textbook kinetics expected for an interface energy driven process. We show this in Fig. 5, right, where we plot the mean channel width (evaluated in the direction parallel to the stress axis) as a function of time, both for the initial 'microstructure preparation' stage where dislocation activity is absent, and then for the three simulations leading to the creep curves in Fig. 5, left. It is evident that, while creep is strongly dislocation density dependent, the coarsening kinetics itself is practically unaffected by dislocation activity.

4.5. Energetic driving forces for directional coarsening

In order to understand how the interplay of external, misfit and dislocation related elastic fields gives rise to directional coarsening, we investigate the spatio-temporal evolution of the resulting contributions to the elastic energy. The stress can be decomposed into $\sigma = \sigma^{\text{ext}} + \sigma^{\text{mis}} + \sigma^{\text{dis}}$, referring to the externally applied stress and the respective solutions of the misfit and dislocation eigenstrain problems, and similarly the local elastic strain is given by $\varepsilon^{\text{el}} = \varepsilon^{\text{ext}} + \varepsilon^{\text{mis}} + \varepsilon^{\text{dis}}$. Accordingly, the elastic energy density $\mathcal{E}^{\text{el}} = \frac{1}{2}\sigma : \varepsilon^{\text{el}}$ can be understood as a sum of 6 contributions:

$$
\begin{aligned}
\mathcal{E}^{\text{el}} &= \mathcal{E}^{\text{ext,ext}} + \mathcal{E}^{\text{ext,mis}} + \mathcal{E}^{\text{ext,dis}} + \mathcal{E}^{\text{mis,dis}} + \mathcal{E}^{\text{mis,mis}} + \mathcal{E}^{\text{dis,dis}} \\
\mathcal{E}^{\text{X,X}} &= \frac{1}{2}\sigma^{\text{X}} : \varepsilon^{\text{X}}, \\
\mathcal{E}^{\text{X,Y}} &= \sigma^{\text{X}} : \varepsilon^{\text{Y}} = \sigma^{\text{Y}} : \varepsilon^{\text{X}}.
\end{aligned}
\tag{22}
$$

where X,Y $\in$ [ext,mis,dis]. The corresponding total (space averaged) energy contributions are denoted as $E^{\text{X,Y}} = \int \mathcal{E}^{\text{X,Y}} dV$. Of these, the energy contribution $\mathcal{E}^{\text{ext,ext}}$ is homogeneous in space and, under creep loading conditions, constant in time; it will therefore not enter our subsequent discussion. Figure 6 shows the spatial patterns formed by the different elastic energy density contributions, both in an unrafted microstructure (Fig. 6(a)) and in a strongly rafted microstructure (Fig. 6(b)). We make the following observations:
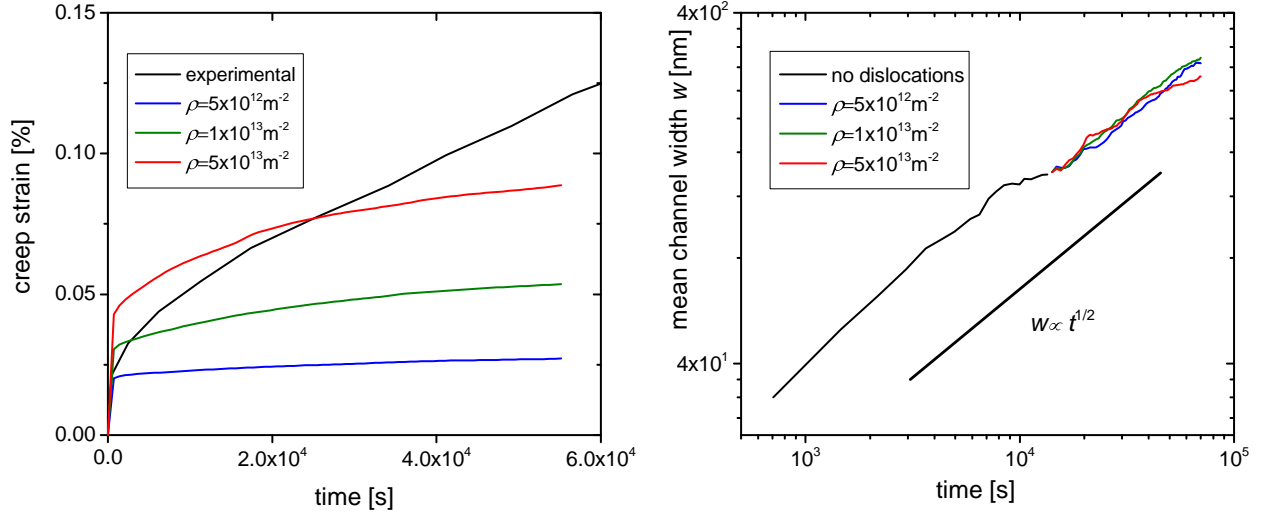
13

Figure 5: Left: Creep curves for different dislocation densities and experimental creep data; right: coarsening kinetics (channel width w vs. time) for different dislocation densities (coloured curves) as well as initial coarsening without dislocations (black curve), full line: $w \propto t^{1/2}$.

- Dislocation related stresses are acting both in the channels perpendicular to the stress axis where they oppose the external stress, and in the precipitates as well as the parallel channels where they add to the external stress. This results in an approximately homogeneous energy contribution which increases in the course of rafting. The interaction energy between external and dislocation stresses is negative in the perpendicular channels, where dislocations relax the external stress, but positive elsewhere (first column in Fig. 6).

- Misfit related stresses lead to an energy density contribution which is everywhere positive, but somewhat lower in the precipitates than in the (vertical or horizontal channels). The misfit stresses add to the external stress in the parallel channels where this interaction further increases the elastic energy density, while the interaction reduces the energy in the precipitates and even more so in the stress-parallel channels (second column in Fig. 6).

- The interaction between misfit and dislocation related stresses leads to an energy reduction everywhere in the microstructure with the exception of the stress-parallel channels.

- The total elastic energy is highest in the channels perpendicular to the stress axis, lower in the precipitates, and lowest in the channels parallel to the stress axis. This net effect results from the fact that the misfit related stresses - which produce this effect - are higher in magnitude than the dislocation related stresses which act in the opposite direction.

At first glance it might seem that these findings indicate that the system might lower its energy by coarsening in the stress-parallel direction, however, this is incorrect: The volume average of $\mathcal{E}^{\mathrm{ext,mis}}$, which is the energy contribution that favors coarsening in the stress-parallel direction, is identically zero and not affected by any microstructure changes. This can easily be seen by noting that the external stress/strain is spatially constant, while the elastic stress/strain due to γ/γ' misfit has because of stress equilibrium (Albenga's law) zero spatial average. Hence, rafting cannot be attributed to the misfit energy asymmetry between channels that are parallel and perpendicular to the stress axis. We note that the same argument applies to the interaction energy $\mathcal{E}^{\mathrm{ext,dis}}$. The misfit energy $\mathcal{E}^{\mathrm{mis,mis}}$ may change but does not distinguish between parallel and perpendicular channels. This leaves a reduction of $\mathcal{E}^{\mathrm{dis,mis}}$ as the only potential driving force for directional coarsening.

Fig. 7 shows the changes of the different elastic energy contributions during rafting, taking the initial unrafted microstructure as the starting point. In line with the above argument, both $\mathcal{E}^{\mathrm{ext,dis}}$ and $\mathcal{E}^{\mathrm{ext,mis}}$ do not change with time. The misfit energy $\mathcal{E}^{\mathrm{mis,mis}}$ increases during directional coarsening, indicating that a
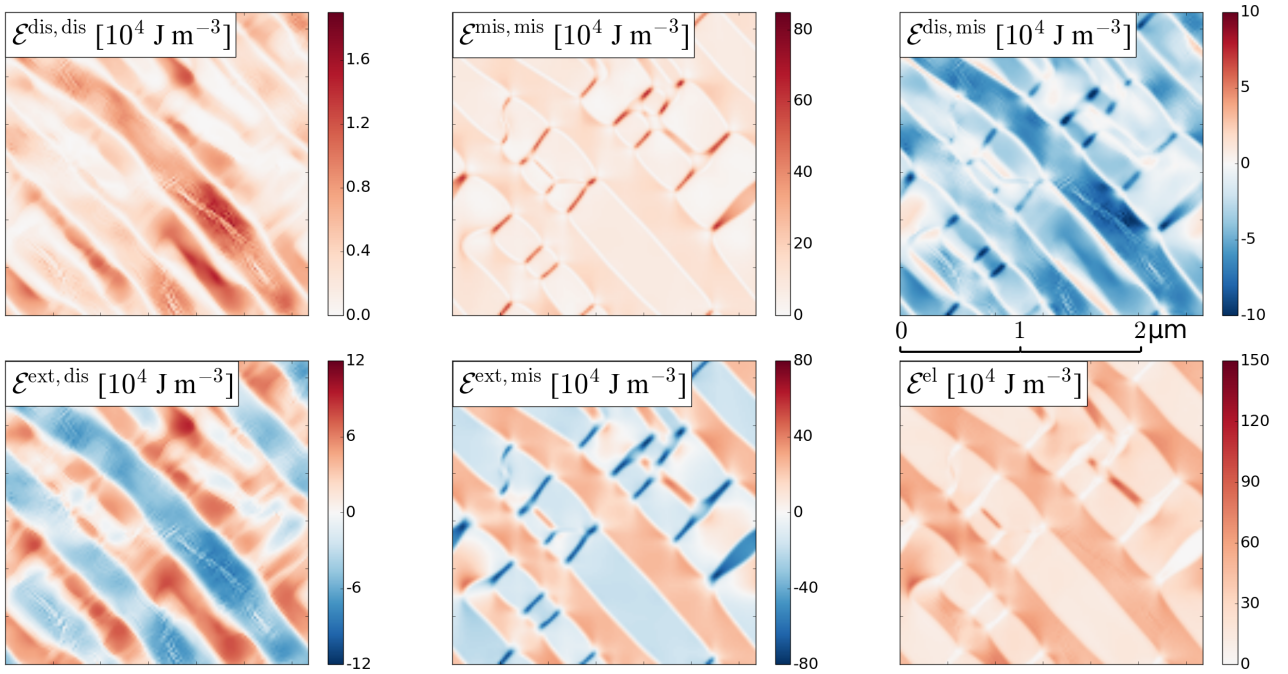
14

(a)
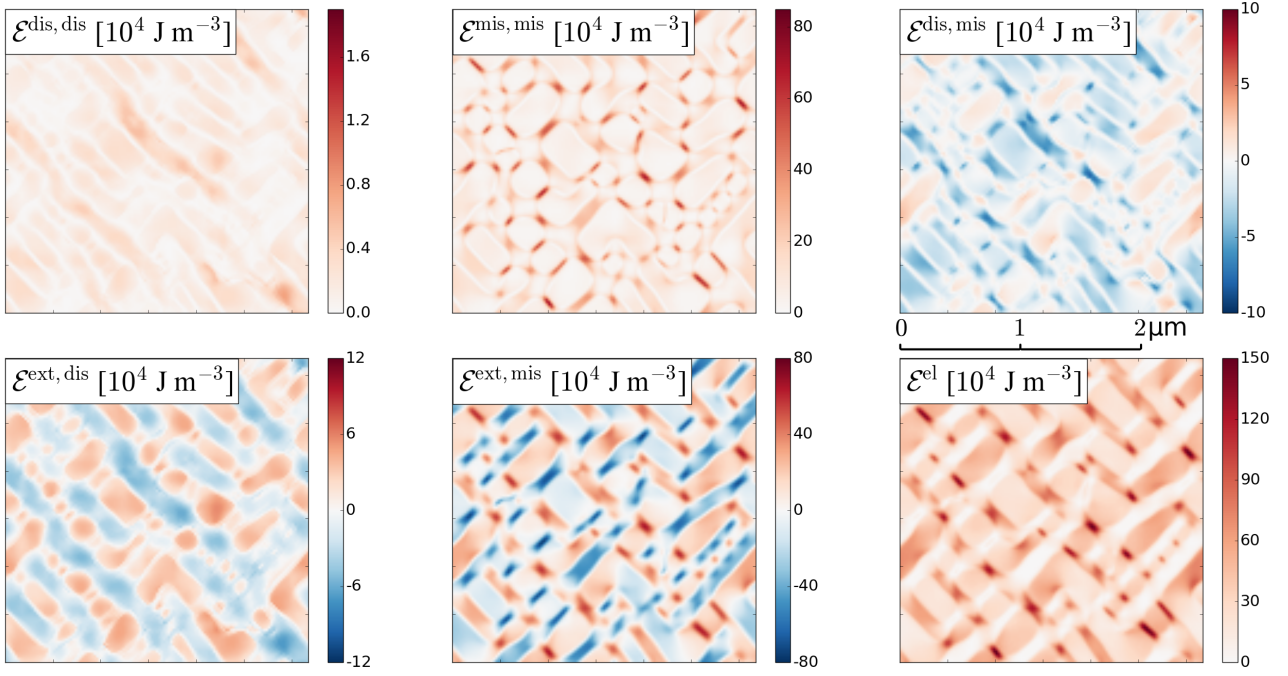
(b)

Figure 6: Elastic energy density contributions, (a) initial unrafted microstructure, (b) strongly rafted microstructure; in both cases energies are computed with quasi-stationary dislocation configurations under load.

15

rafted microstructure provides a less efficient accommodation of misfit stresses if compared to an unrafted one. To understand what provides the driving force for rafting we need to look at the dislocation-related stresses which partly relax the misfit stress in the perpendicular channels, leading to a strong decrease of the corresponding interaction energy which leads to a decrease of the total elastic energy. Thus, we conclude that directional coarsening occurs because the breaking of the symmetry between stress-parallel and stress-perpendicular channels leads to a more efficient plastic relaxation of misfit stresses as compared to a phase microstructure which retains the original cubic symmetry.
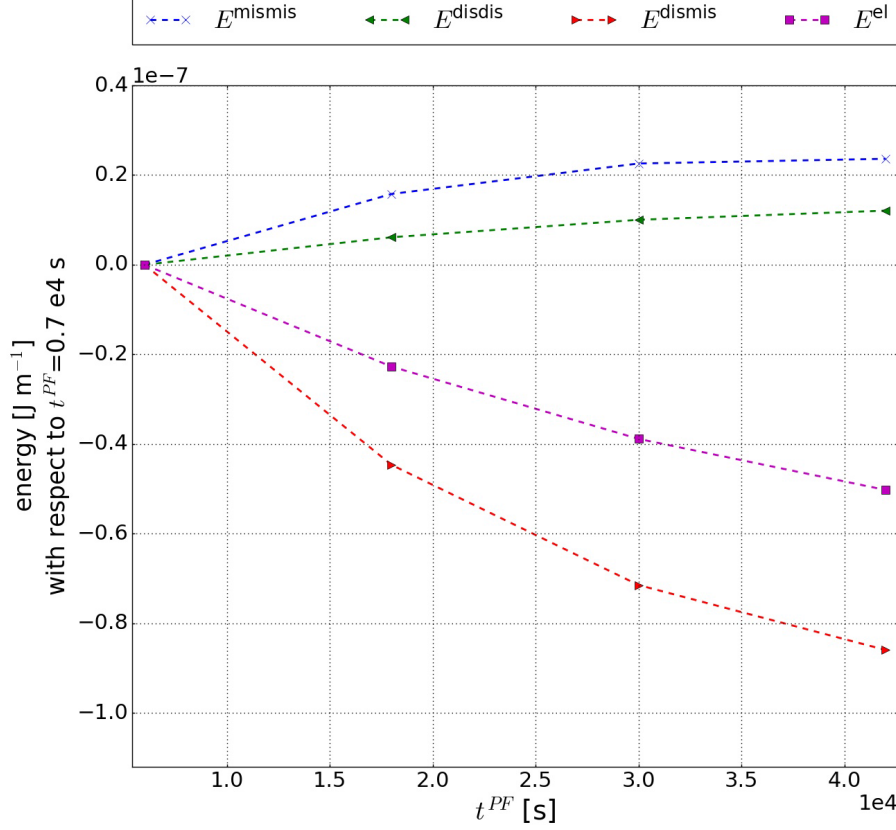

Figure 7: Time evolution of different elastic energy contributions during rafting. The energy contributions $\mathcal{E}^{\text{ext,mis}}$ and $\mathcal{E}^{\text{mis,mis}}$ are constant in time and therefore not included in the figure.

4.6. Microstructure evolution and creep behavior of pre-rafted γ/γ' microstructures

Rafting has a negative effect on creep properties since the rafting process widens – and thereby softens – the channels perpendicular to the tensile stress axis where plastic activity is concentrated. This observation has led to the idea that it might be beneficial to pre-raft γ/γ' microstructures by applying an initial compressive stress, thus reversing the shear stresses and interchanging the role of channels parallel and perpendicular to the stress axis (Mughrabi and Tetzlaff, 2000). Such pre-rafting leads to shrinkage of the channels perpendicular and widening of the channels parallel to the stress axis. If a pre-rafted microstructure is then deformed in tension, the active (stress-perpendicular) channels are initially narrow and thus strong, and one may hope that this has beneficial consequences for the creep properties.

To assess the consequences of pre-rafting in our model, we interchange the roles of stress-parallel and stress-perpendicular channels by simply rotating the stress axis by 90 degrees, halfway into a simulation. In our slip geometry this has exactly the same consequences as a reversal in sign of the axial stress: the resolved shear stresses in the γ channels and hence the direction of creep are reversed. The consequences for the creep behavior are shown in Fig. 8: Upon unloading, we see a small reverse strain caused by the back stresses present in the microstructure. Then, upon re-loading along the new stress axis, we observe a small, quasi-instantaneous deformation as dislocations move under the reversed shear stress. However, in the pre-rafted γ/γ' microstructure this strain is much smaller than the corresponding quasi-instantaneous strain during initial loading of the un-rafted γ/γ' microstructure (compare open circles and open squares in Fig. 8). The reason

16

is obvious: The channels active after stress axis rotation are narrow, and consequentially deformation of these channels induces high back stresses which rapidly cause dislocation activity to stop. In this sense the pre-rafted microstructure fulfills its promise. However, the picture changes as soon as one enters the subsequent stage of co-evolution of the dislocation and phase microstructure: In this stage the rates of the 'backward' creep in the pre-rafted microstructure are much higher than those during the initial, forward creep deformation. This effect is present for all dislocation densities investigated but becomes most pronounced at the highest dislocation density where, despite the small quasi-instantaneous deformation, the reverse strain at the end of the simulation exceeds the deformation accumulated during pre-straining.

Thus we can conclude that the short-term consequences of pre-rafting are beneficial: We find a strongly reduced quasi-instantaneous strain during the initial, dislocation-controlled deformation stage. However, the subsequent creep behavior which is governed by the co-evolution of dislocation and phase microstructure is adversely affected. Because of the mismatch between stress state and microstructure orientation, the thermodynamic driving forces for reconstruction of the phase microstructure are much increased and accordingly this process is significantly accelerated. However, the reconstruction of the phase microstructure goes along with dislocation motions (more so if more dislocations are present) and these motions entail a significantly increased creep activity. Thus, pre-rafting can be envisaged as a double-edged method which, while providing benefits in the short term, may on longer time scales lead to a significant deterioration in creep properties. This observation emphasizes the importance of envisaging dislocation behavior and dislocation creep strain in γ/γ' microstructures not in isolation but always in conjunction with the evolution of the phase microstructure.
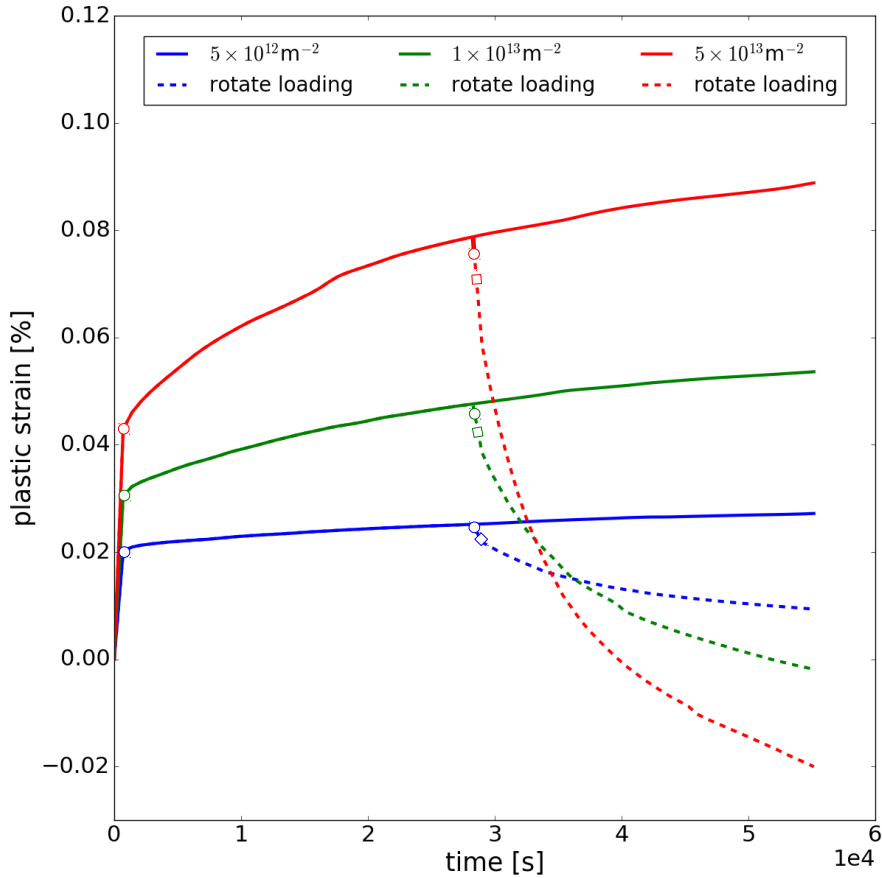

Figure 8: Creep curves for different dislocation densities with change in deformation path (stress axis rotation by 90 degrees) at $t = 28000$ s. Full lines: original stress axis, dashed lines: rotated stress axis. Open circles: quasi-instantaneous strain after loading and unloading along original stress axis; open squares: quasi-instantaneous strain after re-loading along rotated stress axis.

17

5. Discussion of the model

Our model captures essential features of the rafting process driven by the interplay of externally applied stresses, misfit stresses and dislocation related stresses. In particular it demonstrates that no directional coarsening is possible in absence of dislocation activity, which leads to an elastic energy asymmetry between channels parallel and perpendicular to the stress axis that provides the thermodynamic driving force for directional, rather than isotropic coarsening. In this sense we claim that the present model provides us with a minimal model of directional coarsening driven by dislocation plasticity. We also note that the model correctly captures the piling up of dislocations against the phase boundaries. The concomitant forward and back stresses are formally expressed in terms of gradients of the geometrically necessary dislocation density and thus of second-order strain gradients: they introduce an internal length scale into the model (the dislocation spacing) which endows the model with the capability of describing size effects: In our model, narrow channels are stronger than wide channels. The same terms also imply stress concentrations at γ/γ' boundaries which may be essential for understanding why, in later creep stages, dislocations may be able to penetrate the precipitates. Conventional crystal plasticity models without dislocation transport and dislocation-related internal length scales cannot capture these phenomena.

Nevertheless there is ample scope for improving the model. Maybe most conspicuous is the observation that both dislocation multiplication and dislocation recovery are missing from the present formulation. In plane strain simulations considering only edge dislocations, there is strictly speaking no mechanism for multiplication, however, it is common to introduce multiplication through phenomenological ad-hoc rules which are supposed to mimic the action of dislocation sources, see e.g. Yefimov et al. (2004) or Quek et al. (2013). However, dislocation multiplication in γ/γ' microstructures occurs not by sources popping out loops, but rather by moving dislocations expanding in the γ channels and depositing dislocations at the γ/γ' interfaces. Since this process is intimately connected to the motion of dislocations in the heterogeneous phase microstructure, the introduction of dislocation sources through ad-hoc rules may not adequately capture the relevant physical processes and we have refrained from doing so. A more suitable approach, which may provide a both straightforward and promising generalization of the present model, would be to adopt a 3D CDD (or, for the present plane strain problem, a 2.5D CDD) formulation of dislocation kinematics as demonstrated by Monavari et al. (2016) for the general problem of channel slip. More challenging is the inclusion of recovery processes, since recovery in γ/γ' microstructures occurs by climb motion which allows the deposited dislocations to move along the γ/γ' interfaces and ultimately meet recombination partners of opposite sign.

Dislocation recovery by climb leads to a removal of interface dislocations from the system and therefore delimits the internal stresses that build up in the γ channels - in other words, the recovery of dislocations can here lead to a recovery of internal stresses. As a consequence of the interplay between dislocation multiplication, piling up and recovery a dynamic equilibrium might be reached which corresponds to a near-constant creep rate, i.e., secondary creep. The fact that multiplication and recovery are not included restricts our model to the primary creep stage and conversely, an extension to secondary creep will require the incorporation of climb and recovery processes into the model. However, a physically-sound description of dislocation climb is non-trivial: the climb force includes a mechanical contribution from the normal component of the long range elastic stress tensor as well as osmotic contributions associated with local vacancy equilibrium (Geslin et al., 2014, 2015; Haghighat et al., 2013). Similar to the phase microstructure evolution, dislocation climb processes are controlled by diffusion, hence climb and directional coarsening may occur at comparable rates. We will introduce and systematically investigate the role of dislocation climb in our future work in order to enhance the physical predictivity of our multiphysics model and extend its applicability to higher creep stages.

We finally comment on the description of the interactions between phase and defect microstructure in our model. We consider two types of interaction - an elastic interaction due to the superposition of external, misfit and dislocation induced elastic fields, and a kinematic interaction which accounts for the impenetrability of γ' precipitates to dislocations in terms of a reduced (zero) mobility. The latter description has the consequence that, while a γ dislocation cannot move into the γ' phase, a moving γ/γ' phase boundary can move over a γ dislocation which is then incorporated into the γ' precipitate as a pinned dislocation. This is physically not entirely realistic, since incorporation of an ordinary dislocation into a γ' variant necessarily implies creation of an antiphase boundary (APB) and the APB energy provides a very significant driving force which tries to push the dislocation out of the precipitate. This direct energetic coupling between the dislocation fields and the γ' order parameters is at present not included in our model. It might however be essential to include this

aspect if one wants to describe tertiary creep, where dislocations overcome the repulsion due to APB energy and penetrate the precipitates, leading to precipitate shearing, slip localization and failure.

6. Summary

We have developed a multiphysics model coupling a phase-field and a continuum dislocation dynamics model, and have applied this model to study high temperature and low stress creep in single crystal Nickel-based superalloys. The following conclusions can be drawn from the present work:

1. Directional coarsening is driven by the interplay of external stresses, misfit stresses and dislocation-induced stresses. The basic mechanism can be understood as follows: The superposition of misfit and external stress favors slip in the γ channels that are perpendicular but not in those that are parallel to the stress axis. As soon as dislocation activity sets in, the motion of dislocations leads to a relaxation of misfit stresses and hence to a reduction of the elastic energy in the perpendicular channels (note that in the absence of an asymmetry in dislocation activity there is no such energy asymmetry). Widening the perpendicular channels renders this mechanism more efficient and consequentially, the perpendicular channels widen whereas the parallel channels shrink: We see directional coarsening. The present 2D dislocation dynamics model provides a minimal dislocation based theory to capture this phenomenon.

2. Both creep microstructure and creep behavior show significant dislocation density dependence: Higher dislocation density accelerates both rafting and creep deformation.

3. Dislocation and phase microstructure evolution need to be considered in conjunction. Changes in phase microstructure that inhibit dislocation motion in the short term (pre-rafting) may lead to accelerated phase microstructure changes and increased dislocation activity (hence, deterioration in creep resistance) in the long term.

The present model captures the basic mechanisms of rafting and provides an adequate description of the first creep stage. Improvements are still needed to provide a correct description of three-stage creep curves. These improvements concern the inclusion of dislocation multiplication and recovery into the dislocation dynamics, such as to capture the dynamic equilibrium of both processes which leads to a quasi-stationary behavior in secondary creep. Furthermore, an improved description of the interaction between dislocations and the crystallographic order parameters of the γ' phase is needed to correctly describe the interaction of dislocations and precipitates, in particular the possibility for dislocations to penetrate the precipitates at high stresses/high dislocation densities, which is responsible for softening and failure in creep stage III.

References

References

Acharya, A., April 2001. A model of crystal plasticity based on the theory of continuously distributed dislocations. J. Mech. and Phys. Solids 49 (4), 761–784.

Connolly, M., Whittaker, M., Williams, S., 2014. Development of true-stress creep model through analysis of constant-load creep data with application to finite element methods. Mater. Sci. Tech 30 (15), 1899–1904.

Cottura, M., Le Bouar, Y., Finel, A., Appolaire, B., Ammar, K., Forest, S., 2012. A phase field model incorporating strain gradient viscoplasticity: Application to rafting in Ni-base superalloys. J. Mech. Phys. Solids 60 (7), 1243–1256.

Davis, J. (Ed.), 1997. Directionally solidified and single crystal superalloys, Heat Resistant Materials ASM Specialty Handbook. ASM International, Materials Park, OH.

De Rancourt, V., Ammar, K., Appolaire, B., Forest, S., 2016. Homogenization of viscoplastic constitutive laws within a phase field approach. J. Mech. Phys. Solids 88, 291–319.

Finel, A., Rodney, D., 2000. Phase field methods and dislocations. In: MRS Fall Meeting, Boston, MA.

Gao, S., Fivel, M., Ma, A., Hartmaier, A., 2015. Influence of misfit stresses on dislocation glide in single crystal superalloys: A three-dimensional discrete dislocation dynamics study. J. Mech. Phys. Solids 76, 276–290.

Gaubert, A., Le Bouar, Y., Finel, A., 2010. Coupling phase field and viscoplasticity to study rafting in Ni-based superalloys. Philos. Mag. 90 (1-4), 375–404.

Geslin, P.-A., Appolaire, B., Finel, A., 2014. A phase field model for dislocation climb. Appl. Phys. Lett. 104 (1), 011903.

Geslin, P.-A., Appolaire, B., Finel, A., 2015. Multiscale theory of dislocation climb. Phys. Rev. Lett. 115 (26), 265501.

Groma, I., Sep 1997. Link between the microscopic and mesoscopic length-scale description of the collective behavior of dislocations. Phys. Rev. B. 56 (10), 5807–5813.

Groma, I., Csikor, F., Zaiser, M., 2003. Spatial correlations and higher-order gradient terms in a continuum description of dislocation dynamics. Acta Mater 51 (5), 1271–1281.

Groma, I., Zaiser, M., Ispanovity, P. D., 2016. Dislocation patterning in a 2D continuum theory of dislocations. Physical Review B 93, 214110.

Gururajan, M., Abinandanan, T., 2007. Phase field study of precipitate rafting under a uniaxial stress. Acta Mater. 55 (15), 5015–5026.

Haghighat, S. H., Eggeler, G., Raabe, D., 2013. Effect of climb on dislocation mechanisms and creep rates in γ-strengthened Ni base superalloy single crystals: a discrete dislocation dynamics study. Acta Mater. 61 (10), 3709–3723.

Hochrainer, T., Sandfeld, S., Zaiser, M., Gumbsch, P., 2014. Continuum dislocation dynamics: towards a physical theory of crystal plasticity. J. Mech. Phys. Solids 63, 167–178.

Hochrainer, T., Zaiser, M., Gumbsch, P., 2007. A three-dimensional continuum theory of dislocation systems: kinematics and mean-field formulation. Philos. Mag. 87 (8-9), 1261–1282.

Hu, S., Li, Y., Zheng, Y., Chen, L., 2004. Effect of solutes on dislocation motiona phase-field simulation. Int. J. Plast. 20 (3), 403–425.

Huang, M., Zhao, L., Tong, J., 2012. Discrete dislocation dynamics modelling of mechanical deformation of nickel-based single crystal superalloys. Int. J. Plast. 28 (1), 141–158.

Jácome, L. A., Nörtershäuser, P., Heyer, J.-K., Lahni, A., Frenzel, J., Dlouhy, A., Somsen, C., Eggeler, G., 2013. High-temperature and low-stress creep anisotropy of single-crystal superalloys. Acta Mater. 61 (8), 2926–2943.

Khachaturyan, A., 1983. Theory of structural transformations in solids. Wiley, New York.

Kim, S. G., Kim, W. T., Suzuki, T., 1999. Phase-field model for binary alloys. Phys. Rev. E 60 (6), 7186.

Kim, Y.-K., Kim, D., Kim, H.-K., Oh, C.-S., Lee, B.-J., 2016. An intermediate temperature creep model for Ni-based superalloys. Int. J. Plast. 79, 153–175.

Kröner, E., 1958. Kontinuumstheorie der Versetzungen und Eigenspannungen. Springer-Verlag, Berlin.

Le, K., 2016. Three-dimensional continuum dislocation theory. Int. J. Plast. 76, 213 – 230.

Le Graverend, J.-B., Cormier, J., Gallerneau, F., Villechaise, P., Kruch, S., Mendez, J., 2014. A microstructure-sensitive constitutive modeling of the inelastic behavior of single crystal nickel-based superalloys at very high temperature. Int. J. Plast. 59, 55–83.

Link, T., Epishin, A., Brückner, U., Portella, P., 2000. Increase of misfit during creep of superalloys and its correlation with deformation. Acta Mater. 48 (8), 1981–1994.

Miura, N., Kondo, Y., Ohi, N., 2000. The influence of dislocation substructure on creep rate during accelerating creep stage of single crystal nickel-based superalloy, CMSX-4. In: Superalloys 2000. pp. 377–385.

Monavari, M., Sandfeld, S., Zaiser, M., 2016. Continuum representation of systems of dislocation lines: A general method for deriving closed-form evolution equations. J. Mech. Phys. Solids 95, 575–601.

Mughrabi, H., Tetzlaff, U., 2000. Microstructure and high-temperature strength of monocrystalline nickel-base superalloys. Adv. Eng. Mater. 2 (6), 319–326.

Mura, T., 1963. Continuous distribution of moving dislocations. Philos. Mag. 8 (89), 843–857.

Murakumo, T., Kobayashi, T., Koizumi, Y., Harada, H., 2004. Creep behaviour of Ni-base single-crystal super-alloys with various γ volume fraction. Acta Mater. 52 (12), 3737–3744.

Nemat-Nasser, S., Hori, M., 1999. Micromechanics: Overall Properties of Heterogeneous Materials.

Nörtershäuser, P., Frenzel, J., Ludwig, A., Neuking, K., Eggeler, G., 2015. The effect of cast microstructure and crystallography on rafting, dislocation plasticity and creep anisotropy of single crystal Ni-base superalloys. Mat. Sci. Eng. A 626, 305–312.

Nye, J., 1953. Some geometrical relations in dislocated crystals. Acta Metall. 1, 153–162.

Oruganti, R., 2012. A new approach to dislocation creep. Acta Mater. 60 (4), 1695–1702.

Prakash, A., Guenole, J., Wang, J., Müller, J., 2015. Atom probe informed simulations of dislocationprecipitate interactions reveal the importance of local interface curvature. Acta Mater. 92, 33–45.

Probst-Hein, M., Dlouhy, A., Eggeler, G., 1999. Interface dislocations in superalloy single crystals. Acta Mater. 47 (8), 2497–2510.

Quek, S., Ahluwalia, R., Srolovitz, D., 2013. Deconstructing the high-temperature deformation of phase-separating alloys. Model. Simul. Mater. Sci. Eng. 21 (7), 075011.

Reed, R., Matan, N., Cox, D., Rist, M., Rae, C., 1999. Creep of CMSX-4 superalloy single crystals: effects of rafting at high temperature. Acta Mater. 47 (12), 3367–3381.

Rodney, D., Le Bouar, Y., Finel, A., 2003. Phase field methods and dislocations. Acta Mater. 51 (1), 17–30.

Sandfeld, S., Budrikis, Z., Zapperi, S., Castellanos, D. F., 2015a. Avalanches, loading and finite size effects in 2d amorphous plasticity: results from a finite element model. J. Stat. Mech. Theory Exp. 2015 (2), P02011.

Sandfeld, S., Hochrainer, T., Zaiser, M., Gumbsch, P., 2011. Continuum modeling of dislocation plasticity: Theory, numerical implementation, and validation by discrete dislocation simulations. J. Mater. Res. 26 (05), 623–632.

Sandfeld, S., Monavari, M., Zaiser, M., 2013. From systems of discrete dislocations to a continuous field description: stresses and averaging aspects. Model. Simul. Mater. Sci. Eng. 21, 1–22.

Sandfeld, S., Po, G., 2015. Microstructural comparison of the kinematics of discrete and continuum dislocations models. Model. Simul. Mater. Sci. Eng. 23 (8), 085003.

Sandfeld, S., Thawinan, E., Wieners, C., 2015b. A link between microstructure evolution and macroscopic response in elasto-plasticity: Formulation and numerical approximation of the higher-dimensional continuum dislocation dynamics theory. Int. J. Plast. 72, 1–20.

Sedláček, R., Kratochvíl, J., Werner, E., 1Nov-1Dec 2003. The importance of being curved: bowing dislocations in a continuum description. Philos. Mag. 83 (31-34), 3735–3752, autoren (ohne Sonderzeichen): Sedlacek, Kratochvil, Werner.

Tanimoto, T., Moniruzzaman, M., Murata, Y., Miura, N., Kondo, Y., Tsukada, Y., Koyama, T., 2014. Origin of the morphological change from rafted structure to irregular shape of the γ phase in single crystal nickel-based superalloys. Comp. Mater. Sci. 93, 56–61.

Tien, J., Copley, S., 1971. The effect of uniaxial stress on the periodic morphology of coherent gamma prime precipitates in nickel-base superalloy crystals. Metall. Trans. 2 (1), 215–219.

Titus, M. S., Eggeler, Y. M., Suzuki, A., Pollock, T. M., 2015. Creep-induced planar defects in L1 2-containing Co-and CoNi-base single-crystal superalloys. Acta Mater. 82, 530–539.

Tsukada, Y., Murata, Y., Koyama, T., Miura, N., Kondo, Y., 2011. Creep deformation and rafting in nickel-based superalloys simulated by the phase-field method using classical flow and creep theories. Acta Mater. 59 (16), 6378–6386.

Valdenaire, P.-L., Bouar, Y. L., Appolaire, B., Finel, A., 2016. Density-based crystal plasticity : from the discrete to the continuum. Phys. Rev. B 93 (21), 214111.

Wang, J., Osawa, M., Yokokawa, T., Harada, H., Enomoto, M., 2007. Modeling the microstructural evolution of Ni-base superalloys by phase field method combined with CALPHAD and CVM. Comp. Mater. Sci. 39 (4), 871–879.

Wu, R., Sandfeld, S., 2016. Insights from a minimal model of dislocation-assisted rafting in single crystal nickel-based superalloys. Scripta Mater. 123, 42–45.

Wu, R., Sandfeld, S., 2017. A dislocation dynamics-assisted phase field model for nickel-based superalloys: the role of initial dislocation density and external stress during creep. J. Alloys and Comp.In press.

Wu, W.-P., Guo, Y.-F., Wang, Y.-S., Mueller, R., Gross, D., 2011. Molecular dynamics simulation of the structural evolution of misfit dislocation networks at γ/γ' phase interfaces in Ni-based superalloys. Philos. Mag. 91 (3), 357–372.

Wu, X., Wollgramm, P., Somsen, C., Dlouhy, A., Kostka, A., Eggeler, G., 2016. Double minimum creep of single crystal ni-base superalloys. Acta Mater. 112, 242–260.

Xia, S., El-Azab, A., 2015. Computational modelling of mesoscale dislocation patterning and plastic deformation of single crystals. Model. Simul. Mater. Sci. Eng. 23 (5), 055009.

Yashiro, K., Kurose, F., Nakashima, Y., Kubo, K., Tomita, Y., Zbib, H., 2006. Discrete dislocation dynamics simulation of cutting of γ precipitate and interfacial dislocation network in ni-based superalloys. Int. J. Plast. 22 (4), 713–723.

Yefimov, S., Groma, I., Van der Giessen, E., 2004. A comparison of a statistical-mechanics based plasticity model with discrete dislocation plasticity calculations. J. Mech. Phys. Solids 52 (2), 279–300.

Zaiser, M., 2015. Local density approximation for the energy functional of three-dimensional dislocation systems. Phys. Rev. B 92 (17), 174120.

Zhang, X., Deng, H., Xiao, S., Li, X., Hu, W., 2013. Atomistic simulations of solid solution strengthening in Ni-based superalloy. Comp. Mater. Sci. 68, 132–137.

Zhou, N., Shen, C., Mills, M., Wang, Y., 2010. Large-scale three-dimensional phase field simulation of γ'-rafting and creep deformation. Philos. Mag. 90 (1-4), 405–436.

Zhu, J., Wang, T., Zhou, S., Liu, Z., Chen, L., 2004. Quantitative interface models for simulating microstructure evolution. Acta Mater. 52 (4), 833–840.

Zhu, Y., Li, Z., Huang, M., 2013. Atomistic modeling of the interaction between matrix dislocation and interfacial misfit dislocation networks in Ni-based single crystal superalloy. Comp. Mater. Sci. 70, 178–186.